Review article **Open Access**

Alejandro Varas*, Pablo García-González, Johannes Feist, F.J. García-Vidal and Angel Rubio*

Quantum plasmonics: from jellium models to *ab initio* calculations

DOI 10.1515/nanoph-2015-0141
Received November 12, 2015; revised January 25, 2016; accepted February 29, 2016

Abstract: Light-matter interaction in plasmonic nanostructures is often treated within the realm of classical optics. However, recent experimental findings show the need to go beyond the classical models to explain and predict the plasmonic response at the nanoscale. A prototypical system is a nanoparticle dimer, extensively studied using both classical and quantum prescriptions. However, only very recently, fully *ab initio* time-dependent density functional theory (TDDFT) calculations of the optical response of these dimers have been carried out. Here, we review the recent work on the impact of the atomic structure on the optical properties of such systems. We show that TDDFT can be an invaluable tool to simulate the time evolution of plasmonic modes, providing fundamental understanding into the underlying microscopical mechanisms.

Keywords: *ab initio* methods; plasmonics; nanoparticles; optical absorption; TDDFT.

***Corresponding authors: Alejandro Varas,** Nano-Bio Spectroscopy Group and ETSF Scientific Development Centre, Universidad del País Vasco UPV/EHU, CFM CSIC-UPV/EHU, Av. de Tolosa 72, E-20018 Donostia, San Sebastián, Spain, e-mail: alejandro.varas@ehu.eus; and **Angel Rubio,** Nano-Bio Spectroscopy Group and ETSF Scientific Development Centre, Universidad del País Vasco UPV/EHU, CFM CSIC-UPV/EHU, Av. de Tolosa 72, E-20018 Donostia - San Sebastián, Spain; Max Planck Institute for the Structure and Dynamics of Matter and Center for Free-Electron Laser Science, Luruper Chaussee 149, 22761 Hamburg, Germany, e-mail: angel.rubio@mpsd.mpg.de
Pablo García-González: Departamento de Física Teórica de la Materia Condensada and Condensed Matter Physics Center (IFIMAC), Universidad Autónoma de Madrid, E-28049 Cantoblanco, Madrid, Spain; and ETSF Scientific Development Centre, Av. de Tolosa 72, E-20018 Donostia, San Sebastián, Spain
Johannes Feist and F.J. García-Vidal: Departamento de Física Teórica de la Materia Condensada and Condensed Matter Physics Center (IFIMAC), Universidad Autónoma de Madrid, E-28049 Cantoblanco, Madrid, Spain

Edited by Garnett W. Bryant (Guest Editor)

1 Introduction

Localized surface plasmons (LSPs) are collective oscillations of conduction electrons around the surface of a metallic object that arise as a result of a resonant coupling with an external incident electromagnetic (EM) field [1–4]. Such oscillations are driven by the force exerted by the incident field, whereas the restoring force depends very sensitively on electron-electron interactions and on the curvature of the surface. Then, the frequency of the LSP mode will be determined by the strength of electrostatic interactions and by the geometrical details of the metallic particle. It is thus possible to design and fabricate *plasmonic nanostructures* with a range of LSP resonance frequencies that can be determined virtually at will [5]. This tunability is at the heart of plasmonic-based nanoantennas [6, 7] or light-harvesting [8] and sensing devices [9]. In addition, the strong induced charge oscillations emit EM fields that are enhanced and concentrated in subwavelength regions [10, 11], which is the basis of plasmon-enhanced spectroscopies [12, 13]. Plasmon oscillations are also damped through non-radiative channels and, for instance, the generated heat upon LSP excitation can be used in cancer therapy [14, 15]. Furthermore, LSPs can decay by exciting energetic or "hot" electrons [16, 17], which is a useful mechanism in a number of applications such as photocatalysis or the design of novel photovoltaic devices [18].

In many cases of interest, the plasmonic properties of a nanostructure can be theoretically characterized just by solving the classical Maxwell's equations with appropriate boundary conditions. As long as the sizes of the different constituents of the system are large enough, the EM response of each particle can be described by a *local* permittivity, $\epsilon(\omega)$. The conceptual simplicity of this *local-optics approximation* together with the existence of a number of efficient numerical implementations [3, 19, 20] explains its widespread use in theoretical classical plasmonics.

For nanodevices where the separation between metallic constituents [21, 22] and/or their radii of curvature is smaller than a few nanometers [23], the local-optics

approximation breaks down. Then, the intrinsic spatially *non-local* nature of the optical response has to be incorporated into the classical theory. This can be done either by using simplified hydrodynamic models [24, 25] or by defining space-dependent dielectric functions in the metal-dielectric interfaces [26]. Even if such a non-locality is included in a very crude manner, many deficiencies of the standard local-optics approximation are remedied. For instance, unlike the local prescription, these *classical non-local optics* approaches are able to describe the well-known [27] confined longitudinal plasmon resonances [28, 29] and do not show any pathological behavior in the response of two metallic objects in the touching-contact limit [22]. However, the unrealistic sharp boundaries between a metallic object and the surrounding dielectric medium are still kept. That is, classical non-local optics neglect the inhomogeneity of the electron density at the surface of a metal (the so-called electron-density spill-out). As a consequence, features like size-dependent shifts of the main LSP of isolated small nanoparticles [30] or the existence of further surface collective modes that cannot be supported on stepped conduction-electron distributions [31] are beyond the scope of classical non-local theories. Nonetheless, in many practical applications, the above-mentioned limitations are not relevant, so non-local optics can be considered as state of the art in classical plasmonics.

However, there are recent experiments on the optical properties of two metallic objects at subnanometric separation that dramatically differ from the predictions of both local- and non-local optics [32–38]. In this regime, the optical response is affected by the overlap of electron densities of the two nanoparticles and by the establishment of a photoinduced tunnel current between the metals [39–41]. The latter can be treated, even in the realm of local optics, by including effective dielectric media in what are called *quantum-corrected* classical methods [41]; however, the lack of electron-density spill-out is a serious drawback. For such systems, classical methods are thus inapplicable, which has contributed to the emergence of the field of quantum nanoplasmonics [42]. As a consequence, methods like time-dependent density functional theory (TDDFT) [43], hitherto restricted to condensed matter physics and quantum chemistry, are gaining more and more importance in the field of plasmonics.

The outline of this review is as follows. In the next section, we shall briefly describe the theoretical foundations of TDDFT and illustrate its applicability by analyzing the optical absorption of simple model systems. Then, we will summarize our recent research about the impact of the atomic structure in the optical properties of plasmonic nanostructures with subnanometric gaps. The corresponding summary and outlook will close the review.

2 TDDFT and simple-metal nanostructures

2.1 Theoretical background

Electron spill-out and tunneling are basic manifestations of quantum mechanics, which, in principle, can be only extracted from the many-electron wavefunction or approximations thereof. The rationale behind hydrodynamic models is the assumption that the quantum motion of electrons can be addressed just by using density and velocity fields [44]. Note that in standard classical non-local optics, the induced electron density is indeed inhomogeneous but strictly confined into well-defined boundaries. Therefore, just by removing this constraint, we should have a clear improvement upon the present prescriptions of non-local classical optics. The merit of this "self-consistent" hydrodynamic approximation (HA) is not only the approximate inclusion of genuine quantum effects, but also the possibility of solving Maxwell's equations without imposing any boundary condition at metal-dielectric interfaces. The electron density varies smoothly over the whole space, and both Maxwell's equations and the hydrodynamic equation of motion are solved simultaneously. Only very recently, an HA has been presented as a practical tool for the analysis of the optical response from the perspective of classical plasmonics [45]. However, the very same hydrodynamic prescription is well known in condensed matter and cluster physics for a long time [44, 46, 47]. For instance, the photoabsorption spectrum of metal nanoparticles [48, 49], magnetoplasmon excitations [50], and even non-linear ultrafast electron dynamics [51] have already been analyzed under the HA.

The approach to the electron-light interaction in condensed matter physics is rather different. Even if the EM field is considered as a classical entity, theoretical efforts are directed toward the efficient but accurate solution of the quantum many-electron problem. The many-body perturbation theory or TDDFT [43] are the methods of choice in *ab initio* condensed matter physics [52], and the *quantum* plasmon is simply one of the plethora of the elementary excitation processes in many-body systems. A plasmon in an extended system (bulk or surface) consists of a coherent continuous set of single-electron excitations [1, 47, 53, 54]. However, in a localized system where the one-electron

energy levels are discrete, the analysis of collective excitation must be carried out with care. For example, whether a spectral peak in the absorption spectrum of a finite electron system can be labeled as a plasmon or not is still a matter of debate [55–59]. In any case, the quantum picture of the plasmon always relies on its microscopic description (a "bottom-up" procedure), whereas the classical pictures starts from the macroscopic outcome (the induced density), corresponding to a "top-down" approach. From this point of view, HA is an oversimplification of the electron dynamics where single-electron transitions are neglected.

Among the quantum many-body theoretical methods, TDDFT has become the preferred tool to evaluate optical properties in intermediate and large nanosystems (for a detailed discussion on the foundations and applications of TDDFT, see Refs. [52], [60–63]). It has the advantage of describing the correlated dynamics of electrons in terms of independent particles. Therefore, the calculation of the time evolution of many-electron systems is achievable because the complicated many-body features are contained in the so-called exchange-correlation (XC) potential, $v_{XC}(r, t)$.

TDDFT is the formal extension of Hohenberg-Kohn-Sham density functional theory (DFT) [64, 65]. According to DFT, for an N-electron system under the action of an external potential $v_{ext}(\boldsymbol{r})$, we have the three following exact statements: (i) the ground-state electron density, $n_0(\boldsymbol{r})$, unambiguously defines the many-electron ground state $|\Psi_0\rangle$; (ii) there exists an *energy functional* $E[n]$ whose minimum equals the ground-state energy and its reached at $n(\boldsymbol{r})=n_0(\boldsymbol{r})$; (iii) the minimization can be made by defining a fictitious system of independent fermions [the so-called Kohn-Sham (KS) system] whose ground-state density is also $n_0(\boldsymbol{r})$. In Hartree atomic units ($m_e=\hbar=e=1$), the energy functional is

$$E[n]=T_S[n]+W_H[n]+E_{XC}[n]+\int v_{ext}(\boldsymbol{r})n(\boldsymbol{r})\,d\boldsymbol{r}, \tag{1}$$

where $T_S[n]$ is the kinetic energy of a fictitious KS system with density $n(\boldsymbol{r})$, $W_H[n]$ is the *classical* electron-electron interaction energy, $E_{XC}[n]$ is the so-called exchange-correlation (XC) functional, and the last term in the r.h.s. of Eq. (1) is the interaction energy with the external potential. As a consequence, the universal functional $E_{XC}[n]$ contains all the quantum many-body corrections to the classical electron-electron interaction energy and to the kinetic energy of the KS system. By imposing the variational character of $E[n]$, we arrive at the well-known set of self-consistent KS equations for the ground state:

$$(\hat{t}+\hat{v}_{ext}+\hat{v}_{XC}+\hat{v}_H)|\phi_n\rangle=\varepsilon_n|\phi_n\rangle; \tag{2}$$

$$v_{XC}(\boldsymbol{r})=\left.\frac{\delta E_{XC}[n]}{\delta n(\boldsymbol{r})}\right|_{n=n_0},\ v_H(\boldsymbol{r})=\int\frac{n_0(\boldsymbol{r}_1)}{|\boldsymbol{r}-\boldsymbol{r}_1|}d\boldsymbol{r}_1 \tag{3}$$

$$n_0(\boldsymbol{r})=\sum_\sigma\sum_{n=1}^{N}|\phi_n(\boldsymbol{r},\sigma)|^2\ \text{with}\ \varepsilon_1\le\varepsilon_2\le\ldots, \tag{4}$$

where $\hat{t}$ is the one-electron kinetic-energy operator, $|\phi_n\rangle$ are normalized one-electron states, ε_n are their corresponding eigenenergies, and σ is the spin orientation. Hence, the effective one-body potential $\hat{v}_S=\hat{v}_{ext}+\hat{v}_{XC}+\hat{v}_H$ defines the fictitious KS system of N independent fermions. The only unknown ingredient is the XC functional, and practical applications rely on approximations to $E_{XC}[n]$. The success and popularity of KS-DFT is due to the accuracy obtained by using very simple functional forms of $E_{XC}[n]$, like the local-density (LDA) or generalized-gradient (GGA) approximations [60].

Let us suppose that at $t=0$, an external perturbation acts on the many-body ground-state $|\Psi_0\rangle$; that is, for $t\ge0$, the external potential is $v_{ext}(\boldsymbol{r}, t)=v_{ext}(\boldsymbol{r})+\delta v_{ext}(\boldsymbol{r}, t)$. For instance, $\delta v_{ext}(\boldsymbol{r}, t)$ can be the scalar potential of an incident EM field in the quasi-static approximation (i.e. neglecting retardation effects). The Runge-Gross theorem [43] states that, under very general conditions, the dynamical evolution of the system is the direct time-dependent extension of the ground-state KS equations. Namely, the static Schrödinger equation [Eq. (2)] is replaced by its dynamical counterpart

$$(\hat{t}+\hat{v}_{ext}(t)+\hat{v}_{XC}(t)+\hat{v}_H(t))|\phi_n(t)\rangle=\mathrm{i}\frac{d}{dt}|\phi_n(t)\rangle, \tag{5}$$

with the initial conditions $|\phi_n(t=0)\rangle=|\phi_n\rangle$. Here, $v_H(\boldsymbol{r}, t)$ is the classical Coulomb potential generated by the density $n(\boldsymbol{r}, t)$, $v_{XC}(\boldsymbol{r}, t)$ is the XC potential for $n(\boldsymbol{r}, t)$, and the density itself is given by

$$n(\boldsymbol{r}, t)=\sum_\sigma\sum_{n=1}^{N}|\phi_n(\boldsymbol{r}, \sigma; t)|^2. \tag{6}$$

However, the time-dependent XC potential *is not* the functional derivative of any other functional, but actually a functional of all the electron densities at times $t'<t$. Fortunately, such memory effects can be safely neglected when studying the plasmonic response of a nanosystem. This is the so-called *adiabatic* prescription of TDDFT, where $v_{XC}(\vec{r}, t)$ is obtained from the density $n(\vec{r}, t)$ at the same time t from

$$v_{XC}(\boldsymbol{r}, t)\simeq\left.\frac{\delta E_{XC}[n]}{\delta n(\boldsymbol{r})}\right|_{n=n(\boldsymbol{r},t)}, \tag{7}$$

$E_{XC}[n]$ being the XC energy functional used to evaluate the unperturbed ground-state density. If, in addition, $E_{XC}[n]$ is formulated under the LDA or the GGA, we have the so-called adiabatic-LDA (ALDA) or GGA approximations.

In the limit of very weak perturbations (linear response regime), the excitation rate due to an external time-dependent perturbation $\delta v_{ext}(\boldsymbol{r}, \omega)e^{-i\omega t}$ is given by

$$w(\omega)=-2\Im\int \delta v^{*}_{ext}(\boldsymbol{r}, \omega)\delta n(\boldsymbol{r}, \omega)\, d\boldsymbol{r}, \tag{8}$$

where $\delta n(\boldsymbol{r}, \omega)e^{-i\omega t}=n(\boldsymbol{r}, t)-n_0(\boldsymbol{r})$ is the induced density by such a perturbation, and $\Im$ denotes the imaginary part. In this linear regime, the induced density can be written as

$$\delta n(\boldsymbol{r}, \omega)=\int \chi(\boldsymbol{r}, \boldsymbol{r}_1, \omega)\delta v_{ext}(\boldsymbol{r}_1, \omega)d\boldsymbol{r}_1, \tag{9}$$

$\chi(\boldsymbol{r}, \boldsymbol{r}_1, \omega)$ being the density-density response of the unperturbed many-electron ground state $|\Psi_0\rangle$ [66]. However, according to the Runge-Gross theorem, $\delta n(\boldsymbol{r}, \omega)e^{i\omega t}$ is also the induced density of the KS system but due to a perturbation $\delta v_S(\boldsymbol{r}, \omega)e^{-i\omega t}$, which is equal to the external one plus the induced Coulomb and XC potentials. That is,

$$\delta n(\boldsymbol{r}, \omega)=\int \chi_S(\boldsymbol{r}, \boldsymbol{r}_1, \omega)\delta v_S(\boldsymbol{r}_1, \omega)d\boldsymbol{r}_1, \tag{10}$$

where $\chi_S(\boldsymbol{r}, \boldsymbol{r}_1, \omega)$ is the linear response of the KS system of independent electrons, and

$$\delta v_S(\boldsymbol{r}, \omega)=\delta v_{ext}(\boldsymbol{r}, \omega)+\int \frac{\delta n(\boldsymbol{r}, \omega)}{|\boldsymbol{r}-\boldsymbol{r}_1|}d\boldsymbol{r}_1+\delta v_{XC}(\boldsymbol{r}, \omega). \tag{11}$$

The induced XC potential, $\delta v_{XC}(\boldsymbol{r}, \omega)$, is formally given by [67]

$$\delta v_{XC}(\boldsymbol{r}, \omega)=\int K_{XC}(\boldsymbol{r}, \boldsymbol{r}_1, \omega)\delta n(\boldsymbol{r}_1, \omega)d\boldsymbol{r}_1, \tag{12}$$

where $K_{XC}(\boldsymbol{r}, \boldsymbol{r}_1, \omega)$ is the frequency representation of the so-called dynamical XC kernel

$$K_{XC}(\boldsymbol{r}, \boldsymbol{r}_1, t-t_1)=\frac{\delta v_{XC}(\boldsymbol{r}, t)}{\delta n(\boldsymbol{r}_1, t_1)}. \tag{13}$$

On the other hand, the linear response function χ_S can be evaluated in terms of the stationary orbitals $\phi_k(\boldsymbol{r}, \sigma)$ with eigenenergies ε_k of the KS Hamiltonian $\hat{h}_S=\hat{t}+\hat{v}_S$ as follows:

$$\begin{aligned}\chi_S(\boldsymbol{r}_1, \boldsymbol{r}_2, \omega)=&\\ &\sum_{\sigma}\sum_{n=1}^{N}\phi^{*}_n(\boldsymbol{r}_1, \sigma)G^{(\sigma)}_S(\boldsymbol{r}_1, \boldsymbol{r}_2, \varepsilon_n+\omega)\phi_n(\boldsymbol{r}_2, \sigma)\\ &+\sum_{\sigma}\sum_{n=1}^{N}[\phi^{*}_n(\boldsymbol{r}_1, \sigma)G^{(\sigma)}_S(\boldsymbol{r}_2, \boldsymbol{r}_1, \varepsilon_n-\omega)\phi_n(\boldsymbol{r}_2, \sigma)]^{*}\end{aligned} \tag{14}$$

$G^{(\sigma)}_S(\boldsymbol{r}_1, \boldsymbol{r}_2, \Omega)$ being the Green function,

$$\hat{G}^{(\sigma)}_S(\boldsymbol{r}_1, \boldsymbol{r}_2, \Omega)=\sum_k \frac{\phi_k(\boldsymbol{r}_1, \sigma)\phi^{*}_k(\boldsymbol{r}_2, \sigma)}{\Omega-\varepsilon_k+i0^{+}}. \tag{15}$$

Finally, putting together Eqs. (9)–(12), we arrive at a linear equation for the induced density, which, in matrix notation, reads as

$$[1-\hat{\chi}_S(\omega)\hat{K}_{HXC}(\omega)]\delta n(\boldsymbol{r}, \omega)=\hat{\chi}_S(\omega)\delta v_{ext}(\boldsymbol{r}, \omega), \tag{16}$$

where

$$K_{HXC}(\boldsymbol{r}_1, \boldsymbol{r}_2, \omega)=\frac{1}{|\boldsymbol{r}_2-\boldsymbol{r}_1|}+K_{XC}(\boldsymbol{r}_1, \boldsymbol{r}_2, \omega). \tag{17}$$

Once $\delta n(\boldsymbol{r}, \omega)$ has been obtained, the excitation rate is evaluated from Eq. (8) and the energy absorption rate of the system is equal to $\omega\, w(\omega)$.

The excitation rate [Eq. (8)] is singular when ω is equal to an excitation energy Ω of the many-body electron system, and from Eq. (16) we get that Ω must be a zero of the operator $1-\hat{\chi}_S(\omega)\hat{K}_{HXC}(\omega)$. It also means that $\hat{\chi}_S(\omega)\hat{K}_{HXC}(\omega)$ has an eigenvalue equal to 1, which is the basis of TDDFT matrix formulations amenable for quantum chemistry calculations [68, 69]. Also note that in the limit $\hat{K}_{HXC}(\omega)\to 0$ (i.e. in the limit of independent-electron response), those zeros become the poles of $\hat{\chi}_S(\omega)$. The latter are, of course, the one-electron excitation energies $\varepsilon_f-\varepsilon_i$ of the KS system.

We need approximations to $K_{HXC}(\boldsymbol{r}_1, \boldsymbol{r}_2, \omega)$ for practical implementations of linear response TDDFT. Under the adiabatic approximation [Eq. (7)], the memory effects into the XC potential are neglected. In this case, $K_{XC}(\boldsymbol{r}_1, \boldsymbol{r}_2, \omega)$ does not depend on the frequency and is simply given by

$$K_{XC}(\boldsymbol{r}_1, \boldsymbol{r}_2, \omega)=\left.\frac{\delta v_{XC}(\boldsymbol{r})}{\delta n(\boldsymbol{r})}\right|_{n=n(\boldsymbol{r},t)}, \tag{18}$$

and $v_{XC}(\boldsymbol{r})$ can be obtained, for instance, under the LDA. This linear-response ALDA had been already proposed by Zangwill and Solven in 1980 to evaluate the photoabsorption spectra of several rare-gas atoms [70]. The same recipe was applied in seminal works by Eckardt [71] and Puska et al. [72], to study the optical absorption properties of spherical-jellium clusters.

The number of unoccupied KS states entering into the calculation of the Green function [Eq. (15)] is, in general, a critical convergence parameter. However, the evaluation of such an infinite sum can be circumvented for high-symmetry systems by solving the Schrödinger-like equation satisfied by the Green function. Some examples are the already mentioned closed-shell atoms [70] and spherical jellium clusters [71–79], spherical nanoshells [80–82] and

"nanomatryoshkas" [83–85], planar jellium surfaces or slabs [54], jellium nanowires with cylindrical symmetry [86], and also systems with axial symmetry like spherical nanoparticle dimers [39], or ellipsoidal nanorods [87].

2.2 Spherical nanoparticles

Focusing on nanoparticles with spherical symmetry, it is fairly easy to calculate and analyze the optical absorption of simple sp-metal nanoparticles described by the spherical jellium model [71–75]. In general, good agreements with experiments are obtained after replacing the term $i0^+$ of Eq. (15) by a finite contribution $i\eta$ with η~0.1 eV aimed at mimicking non-electronic decay channels (electron-phonon interaction, for instance) and shape/size dispersion in experimental samples [1, 88, 89]. Moreover, the dynamical screening by *d* electrons, which plays a prominent role in the optical absorption of noble-metal particles [30, 54, 90, 91], can be simulated in spherical-jellium calculations by a dielectric background with an appropriate permittivity $\epsilon_b(\omega)$ [cfr. Eq. (26)] [77]. Finally, the combination of effective dielectric media and suitable confining potentials can be used to get insights on the optical properties of doped semiconductor nanocrystals while keeping the simplicity of the spherical jellium model [92].

The TDDFT evaluation of optical absorption spectra of metal nanoparticles containing several thousands of conduction electrons can also be addressed at an affordable computational cost as long as the spherical symmetry is preserved [76, 78–82]. This allows us, for instance, to compare the optical absorption of isolated metal nanoparticles at different size regimes. An example is given in Figure 1, where we depict the ALDA dipole photoabsorption spectra of Na_N spherical jellium clusters with N=92, 1000, and 5000 atoms. The mean density of the jellium positive background is $n_b=3/(4\pi r_s^3)$ with r_s=3.93 Bohr. Therefore, the jellium sphere radii are R=0.94, 2.08, and 3.55 nm for the three clusters, respectively. We have set the damping frequency η to 10 meV for the evaluation of the Green functions. This value is small enough to observe the contribution of individual single-electron excitations to the optical absorption. Finally, an artificial temperature smearing of 50 K has been included in the ground-state KS calculations of the two largest clusters to speed up their convergence. For each frequency of the external *E*-field, $\boldsymbol{E}_{ext}(\boldsymbol{r}, t)=E_0\exp(-i\omega t)\boldsymbol{e}_x$ [i.e. $\delta v_{ext}(\boldsymbol{r}, \omega)=xE_0$], we evaluate the induced density using Eq. (16). The dynamical polarizability is then given by the induced electric dipole divided by the amplitude of the incident *E*-field:

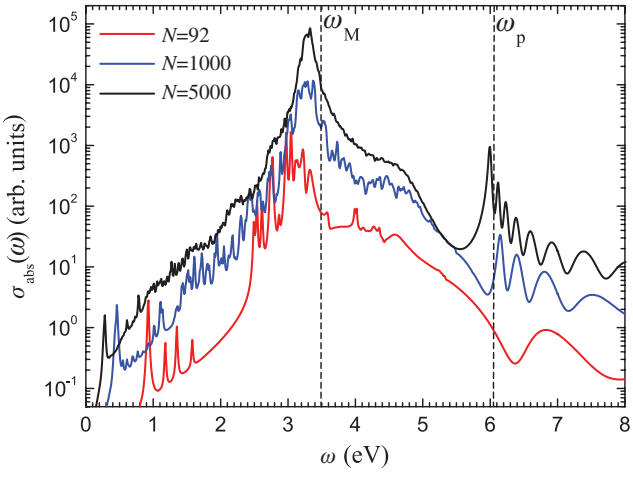

Figure 1: ALDA absorption cross section in arbitrary units for spherical Na_N jellium clusters of radius *R*. Red line: N=92 (R=0.94 nm); blue line: N=1000 (R=2.08 nm); black line: N=5000 (R=3.55 nm). The bulk plasmon frequency, ω_p, and classical Mie dipole surface plasmon frequency, $\omega_M=\omega_p/\sqrt{3}$, are indicated by vertical dashed lines. Note the logarithmic scale of the *y*-axis.

$$\alpha(\omega)=-\frac{1}{E_0}\int x\delta n(\boldsymbol{r}, \omega)d\boldsymbol{r}, \tag{19}$$

whereas the photoabsorption cross-section is given by

$$\sigma_{abs}(\omega)=\frac{4\pi\omega}{c}\Im\alpha(\omega). \tag{20}$$

The general features of the spectrum are very well known [71–73, 88, 89], although it is worthwhile to summarize them. For the smallest cluster (N=92), the presence of the LSP around ω=3 eV is evident, albeit fragmented due to the interaction with surrounding single-electron excitations [93]. In the region around ω=4 eV, a second spectral feature starts to develop, which is a signature of a second surface mode (a Bennett plasmon) resulting from the inhomogeneity of the density profile at the interface [31]. Finally, above the Na volume plasmon frequency $\omega_p\simeq$6.04 eV, a Landau-damped mode clearly emerges in the spectrum: this is a confined longitudinal volume plasmon. The LSP main resonance is red-shifted with respect to the classical value $\omega_M=\omega_p/\sqrt{3}\simeq$3.49 eV simply because the confining potential at the interface is softer than in the classical picture, thus slowing down the oscillations of the electrons. On the contrary, the confined volume mode is blue-shifted with respect to ω_p due to level quantization. That is, for simple sp-metal clusters, there are two competing mechanisms: diffuseness of the confining potential (which dominates for the surface mode) and discreteness of the

one-electron energy levels (which is the most important feature for bulk-like modes) [94]. For the medium-size cluster (N=1000), the LSP frequency approaches to the classical value ω_M and is less fragmented; the Bennett mode is slightly more defined; and not only one but a series of confined volume plasmons appears in the spectrum. Finally, for the largest nanoparticle studied here (N=5000), the one-electron energy levels are very close to be continuous. The LSP comprises almost all the spectral weight, although it still shows a certain structure and its frequency (~3.3 eV) is smaller than ω_M; the Bennett mode appears as a clear shoulder around ω=4.5 eV; and the frequency separation between two consecutive confined volume plasmons is smaller than in Na_{1000}, as expected from the larger size of the cluster. Interestingly, the first confined volume mode appears just *below* ω_p. As for this size the level quantization should not play any role, the diffuseness of the confining potential is the most plausible explanation of this red shift with respect to the classical value.

2.3 Time-propagation TDDFT

For low-symmetry systems, other possibilities exist to circumvent the explicit sum over unoccopied states in the evaluation of the KS system linear response. For instance, by using the Sternheimer method, it is possible to rewrite the response equations in frequency domain in such a way that the explicit use of the virtual KS states is not needed [95]. Another prescription, which is what we follow from now on, is the explicit resolution of the KS time-dependent equations [Eq. (5)] [96]. For instance, if we apply at t=0 a "kick" perturbing potential $\delta v_{ext}(\boldsymbol{r}, t)=\tau_0 v_0(\boldsymbol{r})\delta(t)$, the KS wavefunctions at $t=0^+$ will be

$$\phi_n(\boldsymbol{r}, \sigma; 0^+)=e^{-i\tau_0 v_0(\boldsymbol{r})/\hbar}\phi_n(\boldsymbol{r}, \sigma);\ 1\le n\le N, \tag{21}$$

and for $t>0^+$ the evolution of the KS system can be obtained from Eq. (5) just setting δv_{ext}=0. As

$$\delta v_{ext}(\boldsymbol{r}, t)=\tau_0 v_0(\boldsymbol{r})\delta(t)=\frac{\tau_0}{2\pi}\int_{-\infty}^{+\infty} v_0(\boldsymbol{r})e^{-i\omega t}d\omega, \tag{22}$$

the Dirac-Delta kick is, up to a factor, the superposition of all the monochromatic perturbations $v_0(\boldsymbol{r})\exp(-i\omega t)$. If τ_0 is very small, the linear response theory guarantees that there will be no coupling between the responses due to different frequencies. Therefore, if $\delta n(\boldsymbol{r}, t)$ is the time-dependent induced density given by the time propagation of the KS equations after the Dirac-Delta kick, the density induced by the perturbation $v_0(\boldsymbol{r})\exp(-i\omega t)$ is

$$\delta n(\boldsymbol{r}, \omega)=\frac{1}{\tau_0}\int_0^{+\infty}\delta n(\boldsymbol{r}, t)e^{+i\omega t}dt, \tag{23}$$

as $\delta n(\boldsymbol{r}, t<0)$=0. The corresponding excitation rate [Eq. (8)] is given by

$$w(\omega)=-2\int v_0(\boldsymbol{r})[\Im\delta n(\boldsymbol{r}, \omega)]\,d\boldsymbol{r}, \tag{24}$$

and if $v_0(\boldsymbol{r})=x_i E_0$ (with $i=x, y, z$), the polarizability tensor can be evaluated from

$$\alpha_{ji}(\omega)=-\frac{1}{E_0}\int x_j\delta n(\boldsymbol{r}, \omega)d\boldsymbol{r}. \tag{25}$$

Therefore, the dipole optical-absorption spectrum can be obtained from a single time propagation (or three if we are interested in the full polarizability tensor). The critical convergence parameter is the time-propagation time T_{max} and, in practice, a damping factor $\exp(-\eta t)$ is included into Eq. (25). This damping is completely equivalent to that used to broaden the Dirac-Delta peaks in the calculation of the absorption in the frequency domain. Furthermore, we can calculate explicitly the electron motion under arbitrary time-dependent potentials, not necessarily weak. For instance, the time evolution of the system under quasi-monochromatic pulses and pump-probe laser fields is perfectly achievable. Time propagation is presently implemented in many codes, including *ad hoc* programs aimed at evaluating the optical response of model jellium nanostructures [40, 97, 98]. In what follows, we will use the Octopus package [99–102], which solves the KS time-dependent equations in a real-space representation.

2.4 Nanowire dimers

As a first example of the application of time-propagation TDDFT in model plasmonic nanostructures, let us consider the dipole absorption spectrum for a jellium-Na nanowire of radius R=2 nm and for a nanowire dimer where the separation between jellium boundaries is d=0.5 nm [103]. The incident E-field is perpendicular to the nanowire axis and, in the case of the dimer, it is also parallel to the plane determined by the two cylinder axes (see Figure 2). Unlike other similar studies [97, 98], the only symmetry that is taken into account is the translational invariance along the cylinder axis, which is implemented by imposing Born-von Kármán periodic boundary conditions. The TDDFT results are compared with local and non-local classical predictions, both evaluated using the finite element COMSOL package [104]. For the local calculations, $\epsilon(\omega)$ is a Drude dielectric function

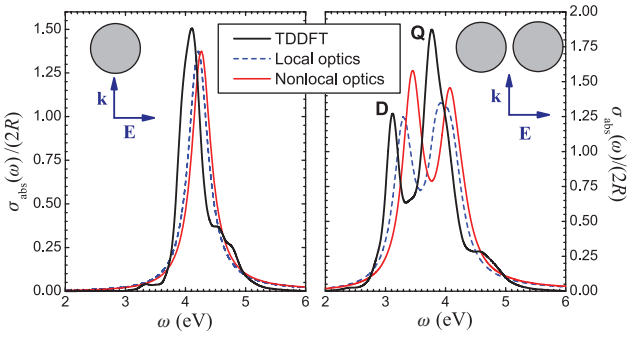

Figure 2: Left panel: Optical absorption spectrum of a sodium nanowire (R=2 nm). Right panel: Optical absorption of a sodium nanowire dimer (R=2 nm, d=0.5 nm). Thick black line: TDDFT; thin blue line: non-local optics; dashed red line: local optics. Both classical calculations have been performed with a damping frequency γ=0.38 eV. Figure adapted from Ref. [103].

$$\epsilon(\omega)=1-\frac{\omega_p^2}{\omega(\omega+i\gamma\omega)}, \tag{26}$$

where ω_p=6.04 eV is the bulk Na plasmon frequency and γ is a phenomenological damping frequency that accounts for non-radiative decay channels for the conduction electrons (for instance, surface scattering) [1]. For the present case, we have chosen γ=0.38 eV. The non-local hydrodynamics calculations are implemented under the prescriptions by Raza et al. and Hiremath et al. [29, 105, 106]. A damping η=0.1 eV is used for the TDDFT calculations. We must note that the distance d=0.5 nm between wires is close to the onset of the establishment of an induced tunnel current between the wires. As mentioned in Section 1, such a current drastically changes the absorption properties of the system. Therefore, we are at the limit of applicability of classical-optics prescriptions.

As can be seen in the left panel of Figure 2, the TDDFT absorption of the single nanowire is dominated by a LSP appearing at $\omega\simeq$4.09 eV. As expected, this value is red-shifted with respect to the classical counterpart $\omega_S=\omega_p/\sqrt{2}\simeq$4.17 eV. The Bennett plasmon appears as a shoulder around $\omega\simeq$4.6 eV, although it is not fully developed in line with the results previously shown for the isolated jellium-Na nanoparticle. Finally, albeit not presented in Figure 2, a series of confined bulk longitudinal plasmons can be observed in the range ω>6 eV [103]. The local-optics absorption consists in a single peak centered at ω_S=4.17 eV corresponding to the main LSP. Such a peak is *blue-shifted* when non-local effects are included, which is the expected result as this standard non-local optics calculation does not describe the electron-density spill-out. Therefore, the local optics spectrum is closer to the TDDFT one due to a cancellation of errors: lack of non-locality and of density spill-out.

The case of the nanowire dimer is more interesting. First, the geometry of the system allows for a very intense enhancement of the E-field in the region between the wires. Second, the absorption spectrum reflects the well-known hybridization of plasmon modes [11, 107, 108]. Higher multipole-order modes in one wire, which cannot be excited by a homogeneous electric field, are excited by the near induced E-field emitted by the other wire and vice versa. This new mode hybridizes with the main dipole plasmon, thus giving a new resonance, which we label as "Q". In addition, the dipole surface plasmons of both wires are coupled and red-shifted with respect to the frequency for an isolated wire, a mode that is noted as "D". It must be mentioned that according to the classical optics picture, the multipole modes of a cylinder are degenerate at a frequency ω_S [47]; that is, all the hybridized modes "depart" from this frequency. Therefore, the spectral feature "Q" might actually contain contributions from higher-order hybridized modes that cannot be resolved in the spectra [97].

As can be observed in the right panel of Figure 2, the description of the absorption spectrum under the three approaches agrees well with the hybridization picture; however, quantitative differences are apparent. Although the distance between the D and Q resonances is practically the same for the three approaches, the relative spectral weight of each resonance as well as the absolute position are very different. Furthermore, the local spectrum shows the prospect of a second hybridization splitting. These discrepancies can be easily traced back to the very different shapes of the induced electron density $\delta n(\boldsymbol{r}, \omega)$. Whereas the quantum TDDFT predicts that it is mainly located outside the jellium boundary, the induced density is concentrated on the surface under the local optics prescription, and $\delta n(\boldsymbol{r}, \omega)$ is spread toward the bulk in the non-local optics approximation. Therefore, the effective electrostatic interaction between the wires is strongest in the quantum picture, whereas it is weakest under non-local optics. Due to the overall dipole symmetry of the induced density along the direction of the incident field, the near E-field emitted by one wire is against the restoring force acting over the induced density in the other wire. Then, the larger the interaction between wires, the less intense the effective restoring force. As a consequence, the red shift of the whole spectrum is strongest in the quantum TDDFT picture. Although the red-shift amount can be easily correlated to the distance between the effective surfaces in both dimers [97], it is evident that

in plasmonic nanostructures with narrow gaps we can only achieve full predictive agreement if the inhomogeneity of the induced density is described properly.

The different shapes of the induced densities will be also reflected on the spatial distribution of the induced electric field enhancement (EFE), defined as the ratio between the amplitudes of the total and the external *E*-fields. In the D mode, where the induced *E*-field is concentrated in the gap region, the overall shape predicted by TDDFT is rather different than the calculated using classical methods (see Figure 3). This is due to the influence of the electron-density spill out. The differences are even larger when considering the Q mode. In this case, there is not even a qualitative agreement between the classical and quantum calculations. This is not a surprise because the higher-order terms in the multipole expansion of the induced density at each wire are more important in the Q mode than in the D resonance. Therefore, the near *E*-field in the Q mode is more sensitive to variations in the shape of the corresponding source. This further confirms that in the limit of subnanometric separations, the inhomogeneity of the density has to be determined accurately when analyzing the plasmonic response of these systems.

3 *Ab initio* nanoplasmonics: Na-cluster dimers

As we have seen in the previous section, the plasmonic response of nanodevices with subnanometric gaps depends very sensitively on the amount of electron-density spill-out in the gap region. Furthermore, as commented in Section 1, the establishment of a photoinduced alternating tunnel current between the metal objects can change even more the absorption properties. Using TDDFT and the jellium model, these effects have been studied in detail in the last years, so the main trends are presently well understood [39, 40, 97, 98, 103]. However, as subnanometric length scales are relevant in these nanodevices, it is expected that the atomic structure around the gap region will have at least quantitative impact. Bearing in mind that one of the ultimate goals in theoretical nanoplasmonic should be the development of robust multiscale methods amenable for addressing both classical and quantum aspects of the optical response [109–111], the quantification of the relevance of the atomic structure in prototypical plasmonic nanodevices is of major importance.

Of course, the atomic structure is routinely taken into account in the analysis and prediction of the properties of metallic clusters either from a quantum-chemistry or a condensed matter perspective [112–115]. Moreover, in the last decade, there has been an increasing interest in the *ab initio* characterization of plasmonic properties of clusters and macromolecules containing up to several hundred atoms. For instance, the plasmon tunability of metallic nanorods and nanowires [116–120], the size-dependent development of collective excitations [121–129], alloys [130–132], core-shell and hybrid nanostructures [133–138], molecular plasmons [55, 139], and small-cluster dimers [140], have been analyzed using TDDFT-based methods. While these studies provide very useful insights about optical absorption properties, only very recently the *ab initio* characterization of other relevant aspects in nanoplasmonics has started to be addressed [141–145].

Sodium-cluster dimers constitute an appropriate play field to address the question about the impact of the atomic structure in nanoplasmonics. Unlike noble metals, the core electrons do not need to be explicitly considered to evaluate the optical response. Therefore, standard norm-conserving pseudopotentials [146] together with the LDA or GGA level of theory can be safely used. By varying the

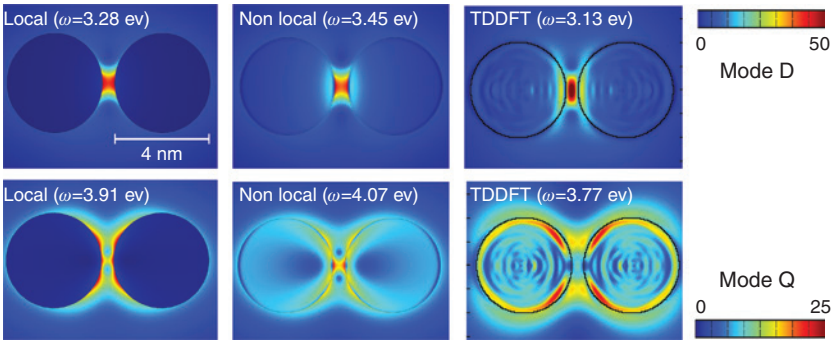

Figure 3: EFE $|\boldsymbol{E}_{tot}(r)|/|\boldsymbol{E}_{ext}|$ corresponding to the dipole (top line) and quadrupole (lower line) resonances of a Na nanowire dimer (d=2 nm). The depicted *E*-fields have been obtained at the frequencies indicated in each panel. Figure adapted from Ref. [103].

cluster-cluster distance, d, different plasmonic regimes can be reached and, therefore, it is possible to carry out a systematic study of the importance of the atomic structure at an acceptable computational cost. Specifically, the calculations that we present in this section [141, 142] were also performed with the Octopus package [99–102]. Typical convergence parameters are spatial-grid spacing of 0.026 nm, total propagation time $T_{max} \simeq 30$ fs, time step $\Delta t = 0.002$ fs, and damping frequency $\eta = 0.1$ eV.

Before analyzing the optical properties of a Na-cluster plasmonic dimer, it is illustrative to discuss very briefly the optical absorption spectra of isolated Na clusters. We consider Na clusters with two different atomic structures: *unrelaxed* bcc-Na_{331}, where the atoms are arranged symmetrically around a central atom on the same bcc lattice as in bulk Na (lattice constant $a = 0.423$ nm), and *relaxed* ico-Na_{297} cluster, which exhibits icosahedral (I_h) symmetry and whose atomic positions are taken from a previous work [147]. Both clusters are almost spherical, and in principle the spherical jellium model is suitable for evaluating their optical properties. Nonetheless, one cannot expect a perfect agreement between the *ab initio* and the jellium-model-based results. The optical properties for the jellium systems are obtained from Octopus as well, although we have checked that for isolated clusters there are minor differences with respect to a homemade code that exploits the full spherical symmetry of those systems. A small temperature smearing has been included in all the calculations.

The comparison of the absorption spectra for the atomistic and the jellium clusters is depicted in Figure 4. As it can be seen, the atom- and jellium-TDDFT spectra

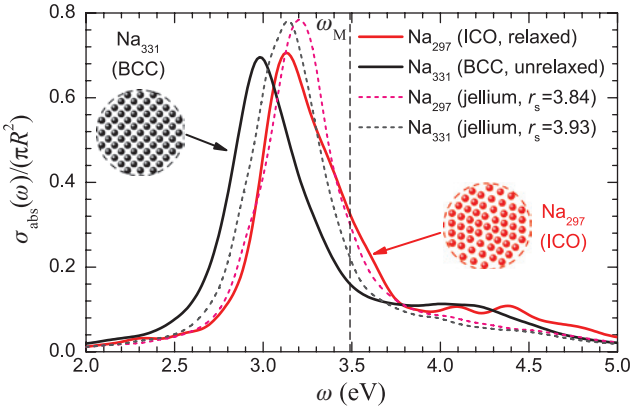

Figure 4: Normalized TDDFT absorption cross section for Na isolated cluster. Solid black line: BCC Na_{331}; solid red line: ICO Na_{297}; black dotted line: jellium Na_{331}; red dotted line: jellium Na_{297}. The classical Mie plasmon frequency for the mean density of bulk Na is indicated by a vertical line. Figure adapted from Ref. [141].

are fairly similar, although the latter are slightly blue-shifted (<0.2 eV). Also note that the whole spectrum of the ico-Na_{297} is blue-shifted with respect to the bcc-Na_{331}. Although a direct comparison is not possible due to the different atomic arrangements, the icosahedral cluster is slightly compressed with respect to the unrelaxed bcc cluster, an effect that we have taken into account in the corresponding jellium calculation. Then, the blue shift of the smallest cluster can be primarily attributed to an overall compression resulting from the relaxation of the structure. As expected from the discussion in the previous section, the four clusters exhibit a spectral feature in the region 4.0–4.5 eV, albeit almost unresolved for the jellium nanoparticles. Nevertheless, none of these qualitative discrepancies are a surprise. In fact, the importance of the atomic structure is manifest when comparing the EFEs. As we may see in Figure 5, the ionic distribution affects the shape of the induced E-field and also its absolute value. Under the jellium model (in what follows, we will only consider the jellium-Na_{331} case), the EFE is overestimated and the tiny structures that reflect the surface corrugation at atomic scale are obviously smoothened out. A more detailed discussion about the inhomogeneities of the induced E-field at atomic scale can be found in the recent work by Barbry et al. [143].

Concerning the response properties of Na-clusters dimers, previous TDDFT studies on spherical-jellium dimers clearly suggest the existence of three distinct separation regimes when the incident E-field is parallel to the dimer axis [39, 40, 148]: (a) classical: at large enough separations, the interaction between clusters is mainly EM as there is a negligible photoinduced charge transfer (CT) between the clusters; (b) intermediate: a tunnelling CT between the clusters appears as a result of a photoinduced alternate voltage bias between the clusters (also note that the ground-state densities of the clusters slightly overlap in this regime); and (c) direct contact: the ground-state densities of the clusters overlap because the Fermi level of the system is above the potential barrier in the dimer junction.

The optical absorption for the three cluster dimers are presented in Figure 6 where we normalize the frequency ω of the incident EM field to the frequency of the Mie LSP $\omega_M^{(i)}$ for each prescription (see Figure 4). By doing so, we will focus on the differences arising from the interaction between the dimers. For $d \gtrsim 0.4$ nm, the three dimers are in the regime (a), and the spectra reflects the hybridization of modes that we described in the previous section. However, there are some differences in the spectra, as the hybridization is strongest in the jellium-Na_{331} dimer and weakest in the ico-Na_{297}, as can be seen in the upper panels

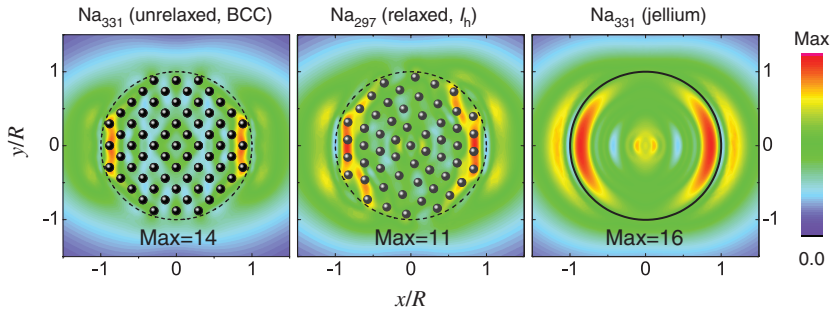

Figure 5: Contour plots of the EFE for the BCC Na_{331}, ICO Na_{297}, and jellium Na_{331} clusters at the corresponding Mie LSP resonance. The *E*-field amplitudes are normalized to their maximum value, which is indicated in each panel. The incident *E*-field is directed along the *X* axis.

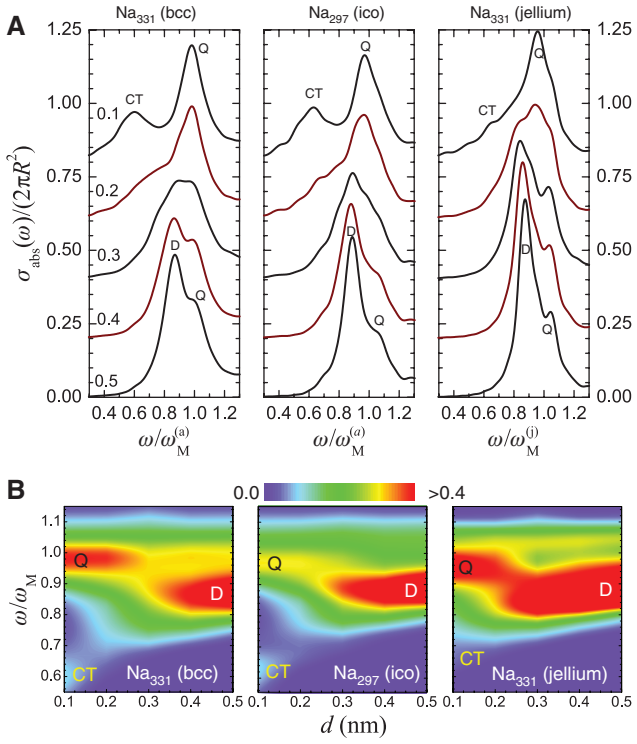

Figure 6: Upper panels: Waterfall representation of the normalized optical absorption cross section for the bcc-Na_{331}, ico-Na_{297}, and jellium-Na_{331} dimers. The spectra have been shifted to ease the comparison between the different regimes. The separation *d* (in Å) is indicated in the left panel. Lower panels: Corresponding contour plots of the normalized absorption spectrum.

of Figure 6. This can be attributed to the different surface shapes of the clusters that affects the EM near field, which, as we know, drives the hybridization process.

In the intermediate regime (b), the classical description breaks down; however, the transition from the classical to this intermediate regime is different in the three dimers (this can be clearly seen in the contour plots displayed the lower panels of Figure 6). For the jellium dimer, the regime (b) is reached at $d \simeq 0.3$ nm. In this case, the D mode frequency stabilizes and the spectral weight of the mode decreases as the nanoparticles approach each other. The hybridized Q mode becomes dominant for $d=0.2$ nm and, finally, when $d=0.1$ nm, the mode D is completely quenched and a very weak signature of a CT mode appears instead [41]. In contrast, the intermediate regime is reached by the atomistic clusters at a larger separation ($d \sim 0.4$ nm), and for $d \simeq 0.1$ nm the CT mode appears as a strong spectral feature in the absorption spectra, this being the signature of the regime (c). It seems that this regime is not fully reached by the jellium cluster in the range of separations that we are considering.

The nanoparticle dimer is one of the prototypical systems to test light-harvesting properties of nanoplasmonic devices. Therefore, it is worth analyzing how the atomistic description affects both the modal shape and EFE associated with the different resonances of the cluster dimer. As we have shown in Figure 6, for $d>0.3$ nm, the optical response of the dimer is dominated by the dipolar mode. In the left panels of Figure 7, we render the electric field amplitudes for this D mode calculated at $d=0.4$ nm for ico-Na_{297} and jellium-Na_{331} dimers (the EFE for the bcc-Na_{331} is very similar to that for the icosahedral-cluster dimer for the four modes depicted in the figure, and it is not included there for the sake of simplicity). As expected, the modal shape is very similar in the three cases, although the D mode for the atomistic cluster is a bit more delocalized than the jellium one. As a consequence, the EFE is reduced by a factor of around 1.5 when considering the atomic structure. For the quadrupole (Q) modes, the relative impact of the atomic structure is greater, and the overestimation of the EFE by the jellium mode persists. Finally, as can be seen in the right panels of Figure 7, the CT mode is not very strongly affected by the atomic structure.

The very different behaviors in the intermediate regime can be easily traced back to the influence that the atomic structure has on the intensity of the photoinduced

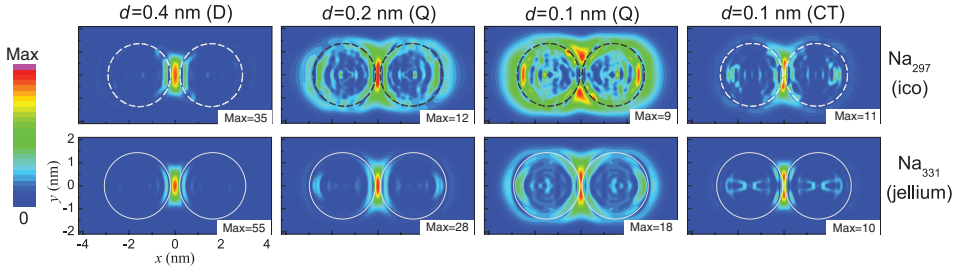

Figure 7: Contour plots of the total electric field amplitude evaluated on the *XY* plane of the dimer at four selected resonances. Upper row: ico-Na_{297}; lower row: jellium-Na_{331}. From left to right: dipolar mode D (d=0.4 nm); quadrupole mode Q (d=0.2 nm), Q mode (d=0.1 nm), and CT mode (d=0.1 nm). In each panel, the *E*-field amplitude is normalized to its maximum value, which is also shown as a legend. Figure adapted from Ref. [141].

current between the particles. However, a direct comparison between the three cases is not entirely possible as there is no way to define a separation d in an unambiguous manner for the three geometries at the same time. A better scenario to quantify the impact of the atomic structure in this model nanoplasmonic structure is to consider only one dimer cluster but changing the relative orientation between the clusters while keeping unchanged the distance between the centers of the nanoparticles. Namely, if $2R$ is the effective diameter of one cluster (2.61 nm for the icosahedral 297-atom nanoparticle), the distance d between the clusters is $d=b-2R$, b being the distance between the center of the clusters (see Figure 8). As the most realistic individual structure is the ico-Na_{297}, in what follows we will restrict our analysis to this cluster. In addition, we will perform some simulations of the plasmon dynamics of the nanostructure [142].

We will address two main features in this analysis: the relative orientation of the clusters and the atomic relaxation due to the mutual interaction. Concerning the former, we treat the two cases represented in Figure 6. The first one leads to a spatial gap that is limited by two 12-atom faces (F2F orientation) and is the geometry that we used in the previous analysis. The second one corresponds to a spatial gap between two three-atom edges (E2E orientation). The first relative orientation maximized the width of the junction but corresponds to a larger separation between atoms. These two effects tend to cancel each other, thus having an stringent but well-defined scenario to quantify in detail the importance of the atomic structure. In addition, the position of the atoms in the junction region is relaxed in the E2E geometry due to the smaller distance between atoms. The energy optimization is performed using the FIRE algorithm [149], recently implemented in Octopus [102]. Once the structure is relaxed, the absorption spectra are calculated as in the previous analysis.

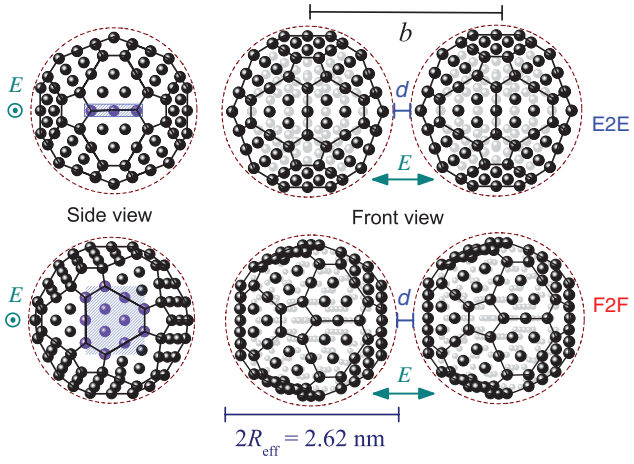

Figure 8: Representation of the two different ico-Na_{297} dimers considered in the present analysis. The applied electric field is orientated along the dimer axis. Figure adapted from Ref. [142].

The dipole optical absorption in the range of separations $0 \le d \le 0.6$ nm is presented in Figure 9. We have also included the optical absorption for the E2E overlapping clusters (d=-0.1 nm), where a major reconstruction of the junction occurs. As can be seen, there are marginal differences between the E2E and F2F optical spectra for the separation regimes (a) and (c), which correspond to the classical and overlapping limits. The irrelevance of the relative orientation in the classical limit is not really surprising due to the overall I_h symmetry of each cluster. In addition, in the overlapping regime (c), the two clusters cannot be considered as individual entities anymore and the system is actually a single "peanut-like" nanoparticle. In fair correspondence with the comparison that we have made for individual clusters, it is not expected that the different arrangements in the junction (which now is inside the nanoparticle) and at the surface will have a major impact in the absorption. As we have already seen, in this overlapping regime, the spectrum is dominated by two LSPs, labeled now as D(CT) and Q(CT), in order to distinguish their shape and emphasize that there is a

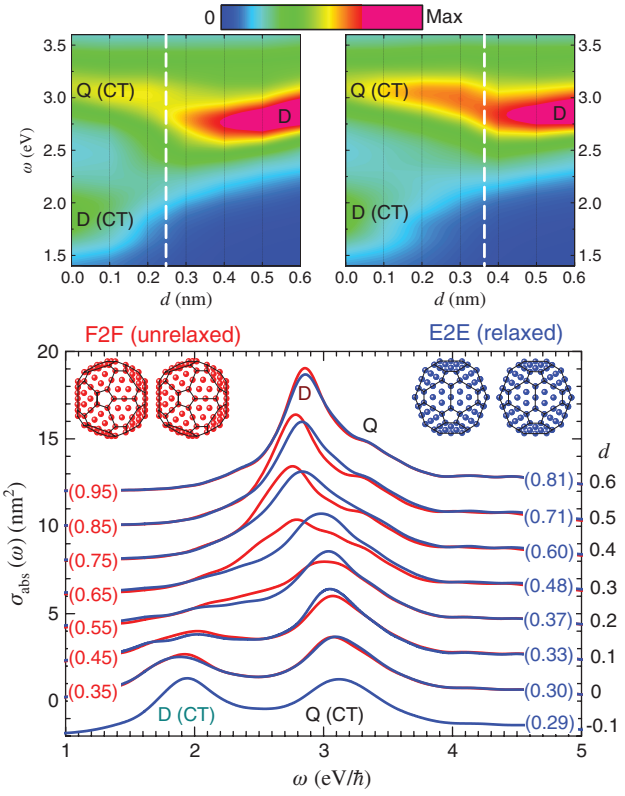

Figure 9: Optical photoabsorption cross sections, $\sigma_{abs}(\omega)$, of Na_{297} dimers as a function of the distance d as defined in the text. Upper panels: contour plots. The vertical dashed line marks the approximate distance where the hybridized Q mode becomes the main spectral feature in the spectrum. Lower panel: waterfall plot of the absorption cross sections. The red and blue lines correspond to the F2F and E2E orientation, respectively. For each distance, the separation in nm between nearest faces or edges is indicated between parenthesis. Figure adapted from Ref. [142].

CT between the two lobes of the peanut-shaped nanoparticle in both modes. Also note that these modes can be addressed using classical optics if the shape of the coalesced nanoparticle is properly modeled [150, 151].

On the contrary, the relative orientation in the intermediate regime (b) is crucial. For this range of distances, the optical absorption of the dimer results from a competition between near induced E-fields and the establishment of a tunneling CT between the nanoparticles. It is evident from Figure 9 that the F2F dimer is not yet in this regime when d~0.4 nm. However, for the E2E dimer, the value of the frequency of the D mode is already locked and there is a net transfer of spectral weight from the D mode to the Q mode, which is a clear signature of the breakdown of the classical picture. In fact, the quantum effects are only discernible in the F2F spectrum when d<0.4 nm. At d=0.3 nm, the two spectra are qualitatively different, as in the E2E dimer the D mode has been already quenched, whereas in the F2F dimer the dipole mode still dominates the spectrum.

Let us remember that the atomic positions of the E2E geometry are relaxed. In fact, the cluster-cluster interaction leading to a further relaxation of the structures with respect to the original energy-optimized ones is only significant if $d\lesssim$0.4 nm for the E2E geometry and if $d\lesssim$0.25 nm for the F2F configuration. For shorter distances, the atomic reconstruction will be important; however, in this regime, the specific ionic arrangement is of secondary importance. Therefore, the atomic relaxation will play a role only in the range of those critical distances where the spectrum changes its overall structure; that is, when the Q mode starts to be dominant. By comparing the absorption spectra depicted in Figure 9 with that obtained without relaxing the atoms in the gap region, we indeed observe a change in the optical spectrum [142]. However, the changes are merely quantitative and less important than those related to the relative orientation.

In Ref. [142], a detailed study of the time evolution of driven induced current intensities and EFEs was presented. In this review, we present some new results that complement those already discussed in Ref. [142]. Specifically, we consider the action over the system of a weak uniform quasi-monochromatic laser pulse of mean frequency ω_{ext} and duration $\tau=20\pi/\omega_{ext}$ (i.e. 10 periods) given by

$$\mathbf{E}(t)=-E_0\sin(\pi t/\tau)\cos(\omega_{ext}t)\mathbf{e}_x, \tag{27}$$

where $E_0=0.51\times10^6$ V m^{-1}. Note that the maximum intensity of this laser pulse is 34.5 kW cm^{-2}, well below the onset of non-linear effects, already analyzed under the jellium model prescription by Marinica and coworkers [40].

As an example of time-resolved dynamics that can be addressed using TDDFT, in Figure 10 we depict the evolution of the x component of the total E-field in the center of the dimer junction driven by the external field [Eq. (27)] and the driven electric dipole,

$$D(t)=-\int x\delta n(\mathbf{r},t)\,d\mathbf{r}, \tag{28}$$

for selected resonant couplings in the E2E nanodimer. For all the cases, as corresponds to the resonance condition, there is a quarter-period phase shift between the external field (represented in the top panel of Figure 10) and the dipole. Moreover, the maximum amplitude of the dipole oscillations are delayed with respect to the maximum intensity of the external field. On the other hand, the different phase shifts between the driven dipole and the E-field can be readily observed. Note that the D mode at d=0.5 nm is the narrowest resonance among all those presented in Figure 10 (see the absorption spectra in Figure 9).

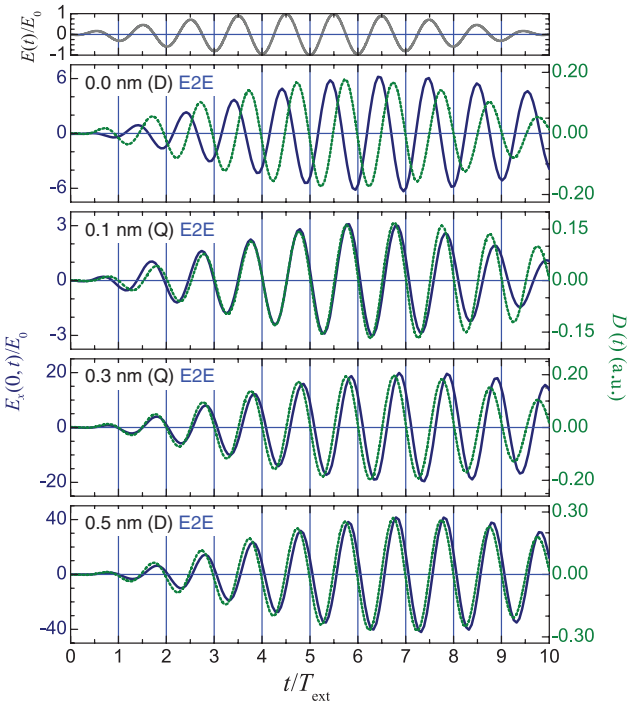

Figure 10: Time evolution of total electric fields (solid blue lines) at the middle of the dimer junction (**r**=0) and induced dipoles (dashed green lines) due to the resonant coupling of selected modes of the E2E nanoparticle dimer with an applied external monochromatic field (depicted in the upper panel) of frequency ω_{ext} and maximum amplitude E_0=10^{-6} a.u.

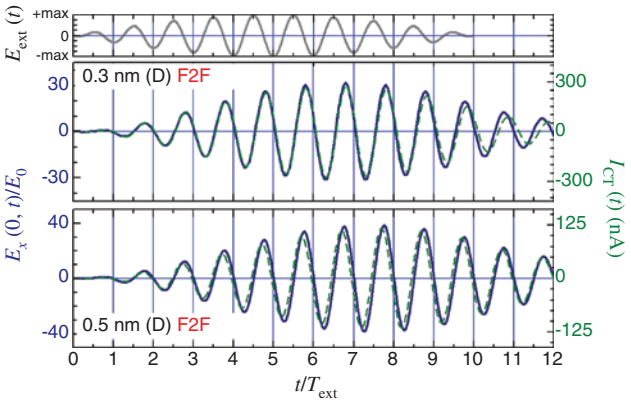

Figure 11: Time evolution of induced currents (dashed green lines) and total electric fields (solid blue lines) at the middle of the dimer junction (**r**=0) due to the resonant coupling of selected modes of the F2F nanoparticle dimer with an applied external monochromatic field (depicted in the upper panel) of frequency ω_{ext} and maximum amplitude E_0=10^{-6} a.u. The subsequent free evolution during a time interval $\Delta T=4\pi/\omega_{ext}$ after the disappearance of the external field is also displayed.

Therefore, when the driving external field starts to fade out, the phase shifts and the relative amplitude between the total E-field and the dipole remain practically the same. However, the relative evolution of these two quantities changes appreciably for the rest of the modes when the intensity of the external perturbation decays.

This effect is easier to observe after the total disappearance of the external field, as the motion of the electrons has to be self-sustained (up to the decay due to the energy transfer from the coherent plasmon mode to an incoherent set of electron-hole excitations), and thus is closer to the actual mode. In Figure 11, we represent the time-resolved evolution of the E-field in the center of the dimer and the current intensity between the nanoparticles for the D modes at d=0.5 nm and d=0.3 nm of the F2F dimer. In both cases, the CT is established via tunneling through the potential barrier between the clusters. Then, the junction behaves in principle as an ohmic resistor [40], which explains the negligible phase shift between the current and the total E-field as well as the practically constant ratio between those quantities. However, upon the disappearance of the driving field, the free evolutions of the induced current and the E-field are not exactly the same when d=0.3 nm, whereas the free evolution seems to be unaffected when d=0.5 nm. The former simply indicates that the self-sustained photoinduced current when d=0.3 nm has to be characterized by an inductive impedance, as it is the case of the modes in the direct-contact regime (c).

4 Outlook and conclusions

TDDFT has been a method of choice in *ab initio* condensed matter and cluster physics for more than two decades. However, its application in nanoplasmonics is far more recent. Quantum simulations not only allow us to explore physical phenomena that cannot be addressed under the classical description of light-matter interaction, but are also an invaluable tool to assess approximate methods. Model calculations, like those discussed in the first part of this review, can be employed for a critical judgment of new theoretical developments with a broader scope of applicability than TDDFT.

We cannot forget that the nanodevices with actual technological interest are much larger than those systems that can be treated in a fully quantum manner. Then, simplified descriptions of the electron motion will be certainly required. For instance, as the limitations of the HA are well known [54], the mere reproduction of the main spectral features of an isolated metallic object in the dipole quasistatic limit is not enough. It would be interesting to perform more stringent assessments of its

predictive accuracy, and the model calculations discussed in this article are indeed a good test. Also note that the HA reduces the many-body problem to a single-body Schrödinger equation, the wavefunction being the square root of the density, so its usefulness in the simulation of dynamical phenomena can be assessed as well.

We have also presented a detailed study of the importance of the atomic structure, so far overlooked in many quantum simulations of the plasmonic response of nanodevices. We have focused on the optical response of a prototypical plasmonic nanostructure and seen that the atomic structure becomes critical in the tunneling CT regime between the constituent nanoparticles. In addition, effects like atomic relaxation and different relative orientations have been also explicitly addressed. On the other hand, our findings confirm the good qualitative accuracy of the jellium model, either combined with quantum mechanical calculations or classical theories, except when there are very narrow gaps in the plasmonic nanostructure. As we have seen, this is precisely the regime where the most complicated processes occur. Thus, we have shown that a fair account of the atomic structure of the junction for very close nanoparticles needs to be taken into account to obtain theoretical results with enough predictive power.

Finally, our calculations of photoinduced currents between nanoparticles constitute a first step toward *ab initio* optoelectronics but at the TDDFT level of theory, which incorporates exchange and correlation quantum many-body effects [152, 153]. In addition, the explicit time propagation of the KS equations enables the time-resolved analysis of the dynamics of the collective motion of electrons driven by an arbitrary external *E*-field. Furthermore, it is possible to simulate the transient regime in the resonant coupling between the nanoparticle and an external quasimonochromatic perturbation, as well as the free evolution of the electron system upon the fade out of the external perturbation. The latter will give us, for instance, first-hand information about plasmon decay via generation of electron-hole pairs. Finally, the frozen-ion approximation, which we have adopted throughout this study, can be relaxed at an affordable computational cost. This paves the way to the semiclassical simulation of other decay channels that are absent in the, until now, few TDDFT simulations in nanoplasmonic devices.

Acknowledgments: We thankfully acknowledge the financial support by the European Research Council (ERC-2010-AdG Proposal No. 267374 and ERC-2011-AdG Proposal No. 290891), the Spanish Government (grants MAT2011-28581-C02-01, FIS2013-46159-C3-1-P, and MAT2014-53432-C5-5-R), the Basque Country Government (Grupos Consolidados IT-578-13), and COST Action MP1306 (EUSpec)]. PGG, JF, and FJGV acknowledge financial support from the Spanish Ministry of Economy and Competitiveness, through the "María de Maeztu" Programme for Units of Excellence in R&D (MDM-2014-0377). We also appreciate the technical support by Joseba Alberdi-Rodrguez and fruitful discussions with Javier Aizpurua, Garnett Bryant, Juan Carlos Cuevas, Stefano Corni, Antonio Fernández-Domnguez, Elisa Molinari, Carmina Monreal, Risto Nieminen, Daniel Sánchez-Portal, Lorenzo Stella, Hans-Christian Weissker, and Pu Zhang.

References

[1] Kreibig U, Vollmer M. Optical properties of metal clusters. Berlin: Springer, 1995.
[2] Maier SA. Plasmonics: fundamentals and applications. New York, NY: Springer, 2007.
[3] Pelton M, Aizpurua J, Bryant G. Metal-nanoparticle plasmonics. Laser Photon Rev 2008;2:136–59.
[4] Pelton M, Bryant G. Introduction to metal-nanoparticle plasmonics. Hoboken, NJ: Wiley, 2013.
[5] Gray SK. Theory and modeling of plasmonic structures. J Phys Chem C 2013;117:1983–94.
[6] Mühlschlegel P, Eisler H-J, Martin OJF, Hecht B, Pohl DW. Resonant optical antennas. Science 2005;308:1607–9.
[7] Giannini V, Fernández-Domínguez AI, Heck SC, Maier SA. Plasmonic nanoantennas: fundamentals and their use in controlling the radiative properties of nanoemitters. Chem Rev 2011;111:3888–912.
[8] Aubry A, Lei DY, Fernández-Domínguez AI, Sonnefraud Y, Maier SA, Pendry JB. Plasmonic light-harvesting devices over the whole visible spectrum. Nano Lett 2010;10:2574–9.
[9] Vo-Dinh T, Dhawan A, Norton SJ, Khoury CG, Wang H-N, Misra V, Gerhold MD. Plasmonic nanoparticles and nanowires: design, fabrication and application in sensing. J Phys Chem C 2010;114:7480–8.
[10] Schuller JA, Barnard ES, Cai W, Jun YC, White JS, Brongersma ML. Plasmonics for extreme light concentration and manipulation. Nat Mater 2010;9:193–204.
[11] Halas NJ, Lal S, Chang W-S, Link S, Nordlander P. Plasmons in strongly coupled metallic nanostructures. Chem Rev 2011;111:3913–61.
[12] Moskovits M. Surface-enhanced spectroscopy. Rev Mod Phys 1985;57:783.
[13] Xu H, Bjeneld E, Käll M, Börjesson L. Spectroscopy of single hemoglobin molecules by surface enhanced Raman scattering. Phys Rev Lett 1999;83:4357–60.
[14] Lal S, Clare SE, Halas NJ. Nanoshell-enabled photothermal cancer therapy: impending clinical impact. Acc Chem Res 2008;41:1842–51.
[15] Huang X, El-Sayed MA. Gold nanoparticles: optical properties and implementations in cancer diagnosis and photothermal therapy. J Adv Res 2010;1:13–28.
[16] Marchuk K, Willets KA. Localized surface plasmons and hot electrons. Chem Phys 2014;445:95–104.

[17] Sundararaman R, Narang P, Jermyn AS, Goddard III WA, Atwater HA. Theoretical predictions for hot-carrier generation from surface plasmon decay. Nat Commun 2014;5:5788.
[18] Clavero C. Plasmon-induced hot-electron generation at nanoparticle/metal-oxide interfaces for photovoltaic and photocatalytic devices. Nat Photonics 2014;8:95–113.
[19] Yang W-H, Schatz GC, Van Duyne RP. Discrete dipole approximation for calculating extinction and Raman intensities for small particles with arbitrary shapes. J Chem Phys 1995;103:869–75.
[20] Taflove A, Hangness SC. Computational electrodynamics: the finite-difference time domain method. Boston, MA: Artech House, 2005.
[21] García de Abajo FJ. Nonlocal effects in the plasmons of strongly interacting nanoparticles, dimers, and waveguides. J Phys Chem C 2008;112:17983–7.
[22] Fernández-Domínguez AI, Wiener A, García-Vidal FJ, Maier SA, Pendry JB. Transformation-optics description of nonlocal effects in plasmonic nanostructures. Phys Rev Lett 2012;108:106802.
[23] Wiener A, Fernández-Domínguez AI, Horsfield AP, Pendry JB, Maier SA. Nonlocal effects in the nanofocusing performance of plasmonic tips. Nano Lett 2012;12:3308–14.
[24] Boardman A. Electromagnetic surface modes. Hydrodynamic theory of plasmon-polaritons on plane surfaces. Chichester: John Wiley & Sons, 1982.
[25] Raza S, Bozhevolnyi SI, Wubs M, Mortensen NA. Nonlocal optical response in metallic nanostructures. J Phys Cond Matter 2015;27:183204.
[26] Luo Y, Fernández-Domínguez AI, Wiener A, Maier SA, Pendry JB. Surface plasmons and nonlocality: a simple model. Phys Rev Lett 2013;111:093901.
[27] Anderegg M, Feuerbacher B, Fitton B. Optically excited longitudinal plasmons in potassium. Phys Rev Lett 1971;27;1565.
[28] Ruppin R. Extinction properties of thin metallic nanowires. Opt Commun 2001;190:205.
[29] Raza S, Toscano G, Jauho A-P, Wubs M, Mortensen NA. Unusual resonances in nanoplasmonic structures due to nonlocal response. Phys Rev B 2011;84:121412(R).
[30] Liebsch A. Surface-plasmon dispersion and size dependence of Mie resonance: silver versus simple metals. Phys Rev B 1993;48:11317–28.
[31] Bennett AJ. Influence of the electron charge distribution on surface-plasmon dispersion. Phys Rev B 1970;1:203–7.
[32] Savage KJ, Hawkeye MM, Esteban R, Borisov AG, Aizpurua J, Baumberg J. Revealing the quantum regime in tunnelling plasmonics. Nature 2012;491:574–7.
[33] Scholl JA, García-Etxarri A, Koh AL, Dionne JA. Observation of quantum tunneling between two plasmonic nanoparticles. Nano Lett 2013;13:564–9.
[34] Tan SF, Wu L, Yang JKW, Bai P, Bosman M, Nijhuis CA. Quantum plasmon resonances controlled by molecular tunnel junctions. Science 2014;343:1496–9.
[35] Cha H, Yoon JH, Yoon S. Probing quantum plasmon coupling using gold nanoparticle dimers with tunable interparticle distances down to the subnanometer range. ACS Nano 2014;8:8554–63.
[36] Kravtsov V, Berweger S, Atkin JM, Raschke MB. Control of plasmon emission and dynamics at the transition from classical to quantum coupling. Nano Lett 2014;14:5270–5.
[37] Zhu W, Crozier KB. Quantum mechanical limit to plasmonic enhancement as observed by surface-enhanced Raman scattering. Nat Commun 2014;5:5228.
[38] Hajisalem G, Nezami MS, Gordon R. Probing the quantum tunneling limit of plasmonic enhancement by third harmonic generation. Nano Lett 2014;14:6651–4.
[39] Zuloaga J, Prodan E, Nordlander P. Quantum description of the plasmon resonances of a nanoparticle dimer. Nano Lett 2009;9:887–91.
[40] Marinica DC, Kazansky AK, Nordlander P, Aizpurua J, Borisov AG. Quantum plasmonics: nonlinear effects in the field enhancement of a plasmonic nanoparticle dimer. Nano Lett 2012;12:1333–9.
[41] Esteban R, Borisov AG, Nordlander P, Aizpurua J. Bridging quantum and classical plasmonics with a quantum corrected model. Nat Commun 2012;3:825.
[42] Tame MS, McEnery KR, Özdemir SK, Lee J, Maier SA, Kim MS. Quantum plasmonics. Nat Phys 2013;9:329–40.
[43] Runge E, Gross EKU. Density-functional theory for time-dependent systems. Phys Rev Lett 1984;52:997–1000.
[44] Lundqvist S. Density Oscillations in Nonuniform Systems. In: Lundqvist S, March NH, eds. Theory of the inhomogeneous electron gas. New York: Plenum, 1983.
[45] Toscano G, Straubel J, Kwiatkowski A, Rockstuhl C, Evers F, Xu H, Mortensen NA, Wubs M. Resonance shifts and spill-out effects in self-consistent hydrodynamic nanoplasmonics. Nat Commun 2015;6:7132.
[46] Eguiluz A, Quinn JJ. Influence of the electron density profile on surface plasmons: retardation effects. Phys Lett A 1975;53:151–3.
[47] Pitarke JM, Silkin VM, Chulkov EV, Echenique PM. Theory of surface plasmon and surface-plasmon polaritons. Rep Prog Phys 2007;70:1–87.
[48] Domps A, Reinhardt P-G, Suraud E. Time-dependent Thomas-Fermi approach for electron dynamics in metal clusters. Phys Rev Lett 1998;80:5520–3.
[49] Banerjee A, Harbola MK. Hydrodynamic approach to time-dependent density functional theory; response properties of metal clusters. J Chem Phys 2000;113:5614–23.
[50] Zaremba E, Tso HC. Thomas-Fermi-Dirac-von Weizsäcker hydrodynamics in parabolic wells. Phys Rev B 1994;49:8147.
[51] Crouseilles N, Hervieux P-A, Manfredi G. Quantum hydrodynamic model for the nonlinear dynamics in thin metal films. Phys Rev B 2008;78:155412.
[52] Onida G, Reining L, Rubio A. Electronic excitations: density-functional versus many-body Green's-function approaches. Rev Mod Phys 2002;74:601.
[53] Pines D. Elementary excitations in solids. New York, NY: Perseus Books, 1999.
[54] Liebsch A. Electronic excitations at metal surfaces. New York, NY: Plenum, 1997.
[55] Bernadotte S, Evers F, Jacob CR. Plasmon in molecules. J Phys Chem C 2013;117:1863–78.
[56] Townsend E, Bryant GW. Which resonances in small metallic nanoparticles are plasmonic? J Opt 2014;16:114022.
[57] Krauter CM, Schirmer J, Jacob CR, Pernpointner M, Dreuw A. Plasmon in molecules: microscopic characterization based on orbital transitions and momentum conservation. J Chem Phys 2014;141:104101.
[58] Guidez EB, Aikens CM. Plasmon resonance analysis with configuration interaction. Phys Chem Chem Phys 2014;16:15501–9.

[59] Jain PK. Plasmon-in-a-box: on the physical nature of few-carrier plasmon resonances. J Phys Chem Lett 2014;5:3112–9.
[60] Fiolhais C, Nogueira F, Marques MAL, eds. A primer in density functional theory. Berlin: Springer, 2003.
[61] Marques MAL, Ullrich CA, Nogueira F, Rubio A, Burke K, Gross EKU, eds. Time-dependent density functional theory. Berlin: Springer, 2006.
[62] Ullrich CA. Time-dependent density functional theory: concepts and applications. Oxford: Oxford University Press, 2011.
[63] Marques MAL, Maitra NT, Nogueira FMS, Gross EKU, Rubio A, eds. Fundamentals of time-dependent density functional theory. Berlin: Springer, 2012.
[64] Hohenberg P, Kohn W. Inhomogeneous electron gas. Phys Rev 1964;136:B864.
[65] Kohn W, Sham LJ. Self-consistent equations including exchange and correlation effects. Phys Rev 1965;140: A1133–8.
[66] Fetter AL, Walecka JD. Quantum theory of many-particle systems. New York: McGraw Hill, 1971.
[67] Petersilka M, Gossmann UJ, Gross EKU. Excitation energies from time-dependent density functional theory. Phys Rev Lett 1996;76:1212–5.
[68] Casida ME. Time-dependent density functional theory for molecules. In: Chong DE, editor. Recent advances in density functional methods. Singapore: World Scientific, 1995.
[69] Grabo T, Petersilka M, Gross EKU. Molecular excitation energies from time-dependent density functional theory. J Mol Struct Theochem 2000;501–2:353–67.
[70] Zangwill A, Soven P. Density-functional approach to local-fields effects in finite systems: photoabsorption in the rare gases. Phys Rev A 1980;21:1561–72.
[71] Eckardt W. Dynamical polarizability of small metal particles: self-consistent spherical jellium background model. Phys Rev Lett 1984;52:1925–28.
[72] Puska MJ, Nieminen RM, Manninen M. Electronic polarizability of small metal spheres. Phys Rev B 1985;31:3486–95.
[73] Ekardt W. Size-dependent photoabsorption and photoemission of small metal particles. Phys Rev B 1985;31:6360–70.
[74] Ekardt W. Collective multipole excitations in small metal particles: critical angular momentum l^{cr} for the existence of collective surface modes. Phys Rev B 1985;32:1961–70.
[75] Beck DE. Self-consistent calculation of eigenfrequencies for the electronic excitations in small jellium spheres. Phys Rev B 1987;35:7325–33.
[76] Cottancin E, Celep G, Lermé J, Pellarin M, Huntzinger JR, Vialle JJ, Broyer M. Optical properties of noble metal clusters as a function of the size: comparison between experiments and a semi-quantal theory. Theor Chem Acc 2006;116:514–23.
[77] Lermé J, Palpant B, Prével B, Pellarin M, Treilleux M, Vialle JL, Perez A, Broyer M. Quenching of the size effects in free and matrix-embedded silver clusters. Phys Rev Lett 1998;80:5105–8.
[78] Lermé J, Baida H, Bonnet C, Broyer M, Cottancin E, Crut A, Maioli P, Del Fatti N, Vallée F, Pellarin M. Size dependence of the surface plasmon resonance damping in metal nanospheres. J Phys Chem Lett 2010;1:2922–8.
[79] Lermé J. Size evolution of the surface plasmon resonance damping in silver nanoparticles: confinement and dielectric effects. J Phys Chem C 2011;115:14098–110.
[80] Prodan E, Nordlander P. Electronic structure and polarizability of metallic nanoshells. Chem Phys Lett 2002;352:140–6.
[81] Prodan E, Nordlander P. Structural tunability of the plasmon resonances in metallic nanoshells. Nano Lett 2003;3:543–7.
[82] Prodan E, Nordlander P, Halas NJ. Electronic structure and optical properties of gold nanoshells. Nano Lett 2003;3:1411–5.
[83] Kulkarni V, Prodan E, Nordlander P. Quantum plasmonics: optical properties of an nanomatryushka. Nano Lett 2013;13:5873–9.
[84] Lin L, Zapata M, Xiong M, Liu Z, Wang S, Xu H, Borisov AG, Gu H, Nordlander P, Aizpurua J, Ye J. Nanooptics of plasmonic nanomatryoshkas: shrinking the size of a core-shell junction to subnanometer. Nano Lett 2015;15:6419–28.
[85] Zapata M, Camacho Beltrán AS, Borisov AG, Aizpurua J. Quantum effects in the optical response of extended plasmonic gaps: validation of the quantum corrected model in core-shell nano nanomatryoshkas. Opt Express 2015;23:8134–49.
[86] Smogunov AN, Kurkina LI, Farberovich OV. Electronic structure and polarizability of quantum metallic wires. Phys Solid State 2000;42:1898–907.
[87] Zuloaga J, Prodan E, Nordlander P. Optical properties and tunability of metallic nanorods. ACS Nano 2010;4:5269–76.
[88] de Heer WA. The physics of simple metal clusters: experimental aspects and simple models. Rev Mod Phys 1993;65:611–76.
[89] Brack M. The physics of simple metal clusters: self-consistent jellium model and semiclassical approaches. Rev Mod Phys 1993;65:677–732.
[90] Tiggesbäumker J, Köller L, Meiwes-Broer K-H, Liebsch A. Blue shift of the Mie plasma frequency in Ag clusters and particles. Phys Rev A 1993;48:R1749(R).
[91] Serra L, Rubio A. Core polarization in the optical response of metal clusters: generalized time-dependent density-functional theory. Phys Rev Lett 1997;78:1428–31.
[92] Zhang H, Kulkarni V, Prodan E, Nordlander P, Govorov O. Theory of quantum plasmon resonances in doped semiconductor nanocrystals. J Phys Chem C 2014;118:16035–42.
[93] Yannouleas C, Vigezzi E, Broglia RA. Evolution of the optical properties of alkali-metal microclusters towards the bulk: the matrix random-phase approximation description. Phys Rev B 1993;47:9849–61.
[94] Monreal RC, Antosiewicz TJ, Apell SP. Competition between surface screening and size quantization for surface plasmons in nanoparticles. N J Phys 2013;15:083044.
[95] Andrade X, Botti S, Marques MAL, Rubio A. Time-dependent density functional theory scheme for efficient calculations of dynamical (hyper)polarizabilities. J Chem Phys 2007;126:184106.
[96] Yabana K, Bertsch GF. Time-dependent local-density approximation in real time. Phys Rev B 1996;54:4484–7.
[97] Teperik TV, Nordlander P, Aizpurua J, Borisov AG. Robust subnanometric plasmon ruler by rescaling of the nonlocal optical response. Phys Rev Lett 2013;110:263901.
[98] Teperik TV, Nordlander P, Aizpurua J, Borisov AG. Quantum effects and nonlocality in strongly coupled plasmonic nanowire dimers. Opt Express 2013;21:27306–25.
[99] Marques MAL, Castro A, Bertsch GF, Rubio A. Octopus: a first-principles tool for excited electron-ion dynamics. Comput Phys Commun 2003;151:60–78.
[100] Castro A, Appel H, Oliveira M, Rozzi CA, Andrade X, Lorenzen F, Marques MAL, Gross EKU, Rubio A. Octopus: a tool for the application of time-dependent density functional theory. Phys Stat Sol B 2006;243:2465–88.

[101] Andrade X, Alberdi-Rodriguez J, Strubbe DA, Oliveira MJT, Nogueira F, Castro A, Muguerza J, Arruabarrena A, Louie SG, Aspuru-Guzik A, Rubio A, Marques MAL. Time-dependent density-functional theory in massively parallel computer architectures: the Octopus project. J Phys Condens Matter 2012;24:233202.
[102] Andrade X, Strubbe D, De Giovannini U, Larsen AH, Oliveira MJT, Alberdi-Rodriguez J, Varas A, Theophilou I, Helbig N, Verstraete MJ, Stella L, Nogueira F, Aspuru-Guzik A, Castro A, Marques MAL, Rubio A. Real-space grids and the Octopus code as tools for the development of new simulation approaches for electronic systems. Phys Chem Chem Phys 2015;17:31371–96.
[103] Stella L, Zhang P, García-Vidal FJ, Rubio A, García-González P. Performance of nonlocal optics when applied to plasmonic nanostructures. J Phys Chem C 2013;117:8941–9.
[104] COMSOL Multiphysics 3.5a. Stockholm: COMSOL AB.
[105] Toscano G, Raza S, Jauho A-P, Mortensen NA, Wubs M. Modified field enhancement in plasmonic nanowire dimers due to nonlocal response. Opt Express 2012;20:4176–88.
[106] Hiremath KR, Zschiedrich L, Schmidt F. Numerical solution of nonlocal hydrodynamic Drude model for arbitrary shaped nano-plasmonic structures using Nédélec finite elements. J Comp Phys 2012;231:5890–6.
[107] Prodan E, Radloff C, Halas NJ, Nordlander P. A hybridization model for the plasmon response of complex nanostructures. Science 2003;302:419–22.
[108] Nordlander P, Oubre C, Prodan E, Li K, Stockman MI. Plasmon hybridization in nanoparticle dimers. Nano Lett 2004;4:899–903.
[109] Lopata K, Neuhauser D. Multiscale Maxwell-Schrödinger modeling: a split field finite-difference time-domain approach to molecular nanopolaritonics. J Chem Phys 2009;130:104707.
[110] Chen H, McMahon JM, Ratner MA, Schatz GC. Classical electrodynamics coupled to quantum mechanics for calculation of molecular optical properties: a RT-TDDFT/FDTD approach. J Phys Chem C 2010;114:14384–92.
[111] Sakko A, Rossi TP, Nieminen RM. Dynamical coupling of plasmons and molecular excitations by hybrid quantum/classical calculations: time-domain approach. J Phys Cond Matt 2014;26:315013.
[112] Bonacic-Koutecky V, Fantucci P, Koutecky J. Quantum chemistry of small clusters of elements of groups Ia, Ib, and IIa: fundamental concepts, predictions, and interpretation of experiments. Chem Rev 19991;91:1035–108.
[113] Daniel M-C, Astruc D. Gold nanoparticles: assembly, supramolecular chemistry, quantum-size-related properties, and applications toward biology, catalysis, and nanotechnology. Chem Rev 2004;104:293–346.
[114] Morton SM, Silverstein DW, Jensen L. Theoretical studies of plasmonics using electronic structure methods. Chem Rev 2011;111:3962–94.
[115] Fernando A, Dimuthu KL, Weerawardene M, Karimova NV, Aikens CM. Quantum mechanical studies of large metal, metal oxide, and metal chalcogenide nanoparticles and clusters. Chem Rev 2015;115:6112–6.
[116] Johnson HE, Aikens CM. Electronic structure and TDDFT optical absorption spectra of silver nanorods. J Phys Chem A 2009;113:4445–50.
[117] Liao M-S, Bonifassi P, Leszczynski J, Ray PC, Huang M-J, Watts JD. Structure, bonding, and linear optical properties of a series of silver and gold nanorod clusters: DFT/TDDFT studies. J Phys Chem A 2010;114:12701–8.
[118] Guidez EB, Aikens CM. Diameter dependence of the excitation spectra of silver and gold nanorods. J Phys Chem C 2013;117:12325–36.
[119] Piccini GM, Havenith RWA, Broer R, Stener M. Gold nanowires: a time-dependent density functional assessment of plasmonic behavior. J Phys Chem C 2013;117:17196–204.
[120] López-Lozano X, Barron H, Mottet C, Weissker H-C. Aspect-ratio- and size-dependent emergence of the surface-plasmon resonance in gold nanorods – an ab initio TDDFT study. Phys Chem Chem Phys 2014;16:1820–3.
[121] Stener M, Nardelli A, De Francesco R, Fronzoni G. Optical excitations of gold nanoparticles: a quantum chemical scalar relativistic time dependent density functional study. J Phys Chem C 2007;111:11862–71.
[122] Joswig J-O, Tunturivuori LO, Nieminen RM. Photoabsorption in sodium clusters on the basis of time-dependent density-functional theory. J Chem Phys 2008;128:014707.
[123] Baishya K, Idrobo JC, Ögüt S, Yang M, Jackson K, Jellinek J. Optical absorption spectra of intermediate-size silver clusters from first principles. Phys Rev B 2008;78:075439.
[124] Aikens CM, Li S, Schatz GC. From discrete electronic states to plasmons: TDDFT optical absorption properties of Ag_n (n = 10, 20, 35, 56, 84, 120) tetrahedral clusters. J Phys Chem C 2008;112:11272–9.
[125] Bae G-T, Aikens CM. Time-dependent density functional theory studies of optical properties of Ag nanoparticles: octahedra, truncated octahedra, and icosahedra. J Phys Chem C 2012;116:10356–67.
[126] Rabilloud F. UV-visible absorption spectra of metallic clusters from TDDFT calculations. Eur Phys J D 2013;67:18.
[127] Li J-H, Hayashi M, Guo G-Y. Plasmonic excitations in quantum-sized sodium nanoparticles studied by time-dependent density functional calculations. Phys Rev B 2013;88:155437.
[128] Weissker H-C, Mottet C. Optical properties of pure and core-shell noble-metal nanoclusters from TDDFT: the influence of the atomic structure. Phys Rev B 2011;84:165443.
[129] Kuisma M, Sakko A, Rossi TP, Larsen AH, Enkovaara J, Lehtovaara L, Rantala TT. Localized surface plasmon resonance in silver nanoparticles: atomistic first-principles time-dependent density-functional theory calculations. Phys Rev B 2015;91:115431.
[130] Barcaro G, Broyer M, Durante N, Fortunelli A, Stener M. Alloying effects on the optical properties of Ag-Au nanoclusters from TDDFT calculations. J Phys Chem C 2011;115:24085–91.
[131] López Lozano X, Mottet C, Weissker H-Ch. Effect of alloying on the optical properties of Ag-Au nanoparticles. J Phys Chem C 2013;117:3062–8.
[132] Rossi TP, Lehtola S, Sakko A, Puska MJ, Nieminen RM. Nanoplasmonics simulations at the basis set limit through completeness-optimized, local numerical basis sets. J Chem Phys 2015;142:094114.
[133] Guidez EB, Mäkinen V, Häkkinen H, Aikens CM. Effects of silver doping on the geometric and electronic structure and optical absorption spectra of the $Au_{25-n}Ag_n(SH)_{18}$ (n = 1, 2, 4, 6, 8, 10, 12) bimetallic nanoclusters. J Phys Chem C 2012;116:20617–24.

[134] Malola S, Lehtovaara L, Enkovaara J, Häkkinen H. Birth of the localized surface plasmon resonance in monolayer-protected gold nanoclusters. ACS Nano 2013;7:10263–70.
[135] Weissker H-Ch, Escobar HB, Thanthirige VD, Kwak K, Lee D, Ramakrishna G, Whetten RL, López-Lozano X. Information on quantum states pervades the visible spectrum of the ubiquitous $Au_{144}(SR)_{60}$ gold nanocluster. Nat Commun 2014;5:3785.
[136] Barcaro G, Sementa L, Fortunelli A, Stener M. Optical properties of silver nanoshells from time-dependent density functional theory calculations. J Phys Chem C 2014;118:12450–8.
[137] Weissker H-Ch, Whetten RL, López-Lozano X. Optical response of quantum-sized Ag and Au cluster-cage vs. compact structures and the remarkable insensitivity to compression. Phys Chem Chem Phys 2014;16:12495–502.
[138] Knoppe S, Häkkinen H, Verbiest T. Nonlinear optical properties of thiolate-protected gold clusters: a theoretical survey of the first hyperpolarizabilities. J Phys Chem C 2015;119:27676–82.
[139] Manjavacas A, Marchesin F, Thongrattanasiri S, Koval P, Nordlander P, Sánchez-Pórtal D, García de Abajo FJ. Tunable molecular plasmons in polycyclic aromatic hydrocarbons. ACS Nano 2013;7:3635–43.
[140] Bae G-T, Aikens CM. TDDFT and CIS studies of optical properties of dimers of silver tetrahedra. J Phys Chem A 2012;116:8260–9.
[141] Zhang P, Feist J, Rubio A, García-González P, García-Vidal FJ. Ab initio nanoplasmonics: the impact of atomic structure. Phys Rev B 2014;90:161407(R).
[142] Varas A, García-González P, García-Vidal FJ, Rubio A. Anisotropy effects on the plasmonic response of nanoparticle dimers. J Phys Chem Lett 2015;6:1891–8.
[143] Barbry M, Koval P, Marchesin F, Esteban R, Borisov AG, Aizpurua J, Sánchez-Portal D. Atomistic near-field nanoplasmonics: reaching atomic-scale resolution in nanooptics. Nano Lett 2015;15:3410–9.
[144] Rossi TP, Zugarramurdi A, Puska MJ, Nieminen RM. Quantized evolution of the plasmonic response in a stretched nanorod. Phys Rev Lett 2015;115:236804.
[145] Marchesin F, Koval P, Barbry M, Aizpurua J, Sanchez-Portal D. Plasmonic response of metallic nanojunctions driven by single atom motion: quantum transport revealed in optics. ACS Photon 2016;3:269–77.
[146] Troullier N, Martins JL. Efficient pseudopotentials for plane-wave calculations. Phys Rev B 1991;43:1993–2006.
[147] Noya EG, Doye JPK, Wales DJ, Aguado A. Geometric magic numbers of sodium clusters: interpretation of the melting behaviour. Eur Phys J D 2007;43:57–60.
[148] Esteban R, Zugarramurdi A, Zang P, Nordlander P, García-Vidal FJ, Borisov AG, Aizpurua J. A classical treatment of optical tunneling in plasmonic gaps: extending the quantum corrected model to practical situations. Faraday Discuss 2015;178:151–83.
[149] Bitzek E, Koskinen P, Gähler F, Moseler M, Gumbsch P. Structural relaxation made simple. Phys Rev Lett 2006;97:170201.
[150] Romero I, Aizpurua J, Bryant GW, García de Abajo FJ. Plasmons in nearly touching metallic nanoparticles: singular response in the limit of touching dimers. Opt Express 2006;14:9988–99.
[151] Lei DY, Aubry A, Luo Y, Maier SA, Pendry JB. Plasmonic interaction between overlapping nanowires. ACS Nano 2011;5:597–607.
[152] Marinica DC, Zapata M, Nordlander P, Kazansky AK, Echenique PM, Aizpurua J, Borisov AG. Active quantum plasmonics. Sci Adv 2015;1:e1501095.
[153] Varas A, García-González P, Garca-Vidal FJ, Rubio A. Unpublished.